AGU PUBLICATIONS

JGR

Journal of Geophysical Research: Oceans

RESEARCH ARTICLE

10.1002/2015JC011140

Special Section:
Physical Processes Responsible for Material Transport in the Gulf of Mexico for Oil Spill Applications

Ocean processes underlying surface clustering

Gregg A. Jacobs[1], Helga S. Huntley[2], A. D. Kirwan Jr.[2], Bruce L. Lipphardt Jr.[2], Timothy Campbell[1], Travis Smith[1], Kacey Edwards[1], and Brent Bartels[3]

[1]Naval Research Laboratory, Stennis Space Center, Mississippi, USA, [2]School of Marine Science and Policy, University of Delaware, Newark, Delaware, USA, [3]VENCOR

Abstract Ageostrophic ocean processes such as frontogenesis, submesoscale mixed-layer instabilities, shelf break fronts, and topographic interactions on the continental shelf produce surface-divergent flows that affect buoyant material over time. This study examines the ocean processes leading to clustering, i.e., the increase of material density over time, on the ocean surface. The time series of divergence along a material trajectory, the Lagrangian divergence (LD), is the flow property driving clustering. To understand the impacts of various ocean processes on LD, numerical ocean model simulations at different resolutions are analyzed. Although the relevant processes differ, patterns in clustering evolution from the deep ocean and the continental shelf bear similarities. Smaller-scale ocean features are associated with stronger surface divergence, and the surface material clustering is initially dominated by these features. Over time, the effect of these small-scale features becomes bounded, as material traverses small-scale regions of both positive and negative divergence. Lower-frequency flow phenomena, however, continue the clustering. As a result, clustering evolves from initial small-scale to larger-scale patterns.

Key Points:
- Ocean processes generate surface divergence that changes surface material density
- Smaller-scale processes have stronger divergence, and initially are the dominant impact
- Larger-scale processes continue material density change at longer time scales

Correspondence to:
G. A. Jacobs,
gregg.jacobs@nrlssc.navy.mil

Citation:
Jacobs, G. A., H. S. Huntley, A. D. Kirwan, B. L. Lipphardt, T. Campbell, T. Smith, K. Edwards, and B. Bartels (2015), Ocean processes underlying surface clustering, *J. Geophys. Res. Oceans*, *120*, doi:10.1002/2015JC011140.

Received 14 JUL 2015
Accepted 4 DEC 2015
Accepted article online 13 DEC 2015

1. Introduction

Sargassum, oil from seeps and spills, and debris often collect in irregular distribution patterns on the ocean surface (Figure 1). These patterns typically consist of patches of buoyant material in high concentrations or "clusters" interspersed with large areas of voids. A particularly impressive display of this behavior resulted from the Deepwater Horizon oil spill in the northeastern Gulf of Mexico (GoM) in 2010 [*Jones et al*., 2011] (see also Figure 1b). Such features are regularly observed from satellites, aircraft, and ships [*Gower et al*., 2006; *Munk et al*., 2000; *Yoder et al*., 1994]. Analogous structures are also observed in estuaries and rivers [*Handler et al*., 2001; *Mied et al*., 2002, 2000]. At the largest scales, clusters include such phenomena as the "great garbage patches" in the ocean gyres driven by convergent surface Ekman currents [*Maximenko et al*., 2012].

Huntley et al. [2015] examine surface material deformation leading to clusters and demonstrate that the underlying divergence is the source. More specifically, the integral of the time series of the horizontal divergence and convergence experienced by material elements as they move through the flow field is found to be the critical diagnostic for cluster formation. We call this along-trajectory time series Lagrangian divergence (LD). Our principal goal here is to understand the ocean processes underlying clustering and their effects on clustering over time. The question thus is what ocean processes control the LD.

A wide range of dynamical processes may contribute to surface divergence and cluster formation. Clusters in rivers and estuaries occur at very large Rossby number, while the great garbage patches are subject to low Rossby number dynamics. The connection between clustering and convergence has been verified at the far ends of the length-scale spectrum: in small-scale turbulent flows [*Schumacher and Eckhardt*, 2002] and in the formation of large garbage patches [*van Sebille et al*., 2012].

Here our focus is on clustering in the submesoscale to mesoscale range (500 m to 500 km) across the deep ocean and continental shelf. *McWilliams* [2008] identified the submesoscale region as the "borderlands" where both Rossby and Froude numbers are of order 1. This is a pivotal region as it lies between the inverse energy cascade at larger scales and the forward cascade at smaller scales. It is home to a variety of nonlinear mechanisms at a large range of spatial and temporal scales. These contribute to cluster formation, subsequent advection, deformation, and dispersal.

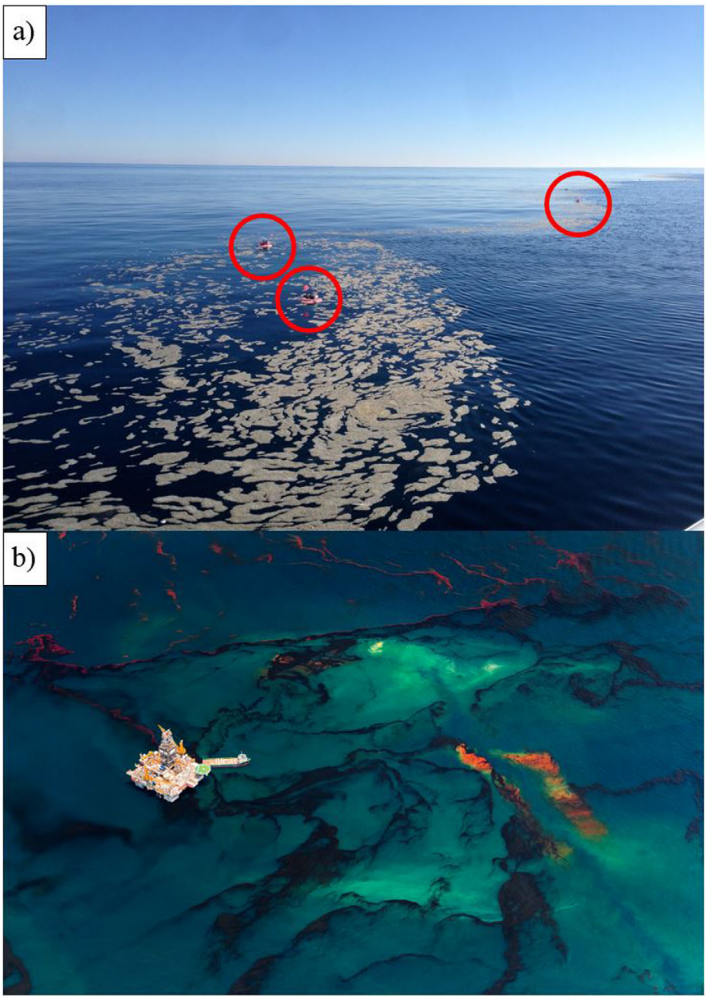

Figure 1. (a) Surface convergence of naturally occurring material and drifting instruments (circled in red) at 30.33°N 86.6°W on 17 December 2013. (Photo by Tamay Özgökmen.) (b) Enhanced image of surface oil distribution following the Deep water Horizon oil spill in 2010. (Photo by Daniel Beltrá.)

Two regions in the GoM are used as test beds. The Grand Lagrangian Deployment (GLAD) field campaign during July 2012 documented substantial submesoscale activity in the northeastern GoM [*Poje et al*., 2014]. Thus, the GLAD area and time period are chosen to examine deep ocean process effects on LD. The Surfzone Coastal Oil Pathways Experiment (SCOPE) during December 2013 aimed to examine the processes on the continental shelf, suggesting a region and time period in shallower waters. We use a series of numerical ocean model experiments with increasing resolutions, each of which captures a different spectrum of phenomena. This permits a systematic investigation of processes operating over relevant scales.

The larger domain, tested at both 3 and 1 km resolution, covers the entire GoM. Nested inside the 1 km setup is a 250 m resolution model, and nested within this is a 50 m resolution setup. Mesoscale phenomena are well depicted in the 3 km setup, with submesoscale instabilities represented at 1 km, energetic shelf break instabilities, and bathymetric interactions in the 250 m model, and further refinement in the bottom interactions in the 50 m model.

The balance of the paper is organized as follows. The next section begins with an example and considers how LD is related to clustering. Section 3 gives model details. Section 4 characterizes the physical processes represented in the model hierarchy and acting on different scales. The subsequent section presents the results of the clustering analyses. The paper concludes with a summary of essential results and a discussion of some of the implications of this research.

2. Clustering Quantification and Evolution

As a first clustering example, we consider the evolution of a set of particles initially distributed with uniform 100 m separation and with trajectories computed from the surface currents of the 250 m resolution model described in more detail in section 3. After 12 h, areas of dense particle clusters appear (Figure 2a), and from this distribution, we compute a cluster strength function as

$$C(x,y)=\sum_{i=1}^{N}\exp\left(-\left((x-x_i)^2+(y-y_i)^2\right)/L^2\right), \quad (1)$$

where (x_i, y_i) is the position of the ith particle out of N, and L is set to 500 m (Figure 2b). Clearly, the cluster strength function shows alternating areas of higher and lower density, indicating clustering. The

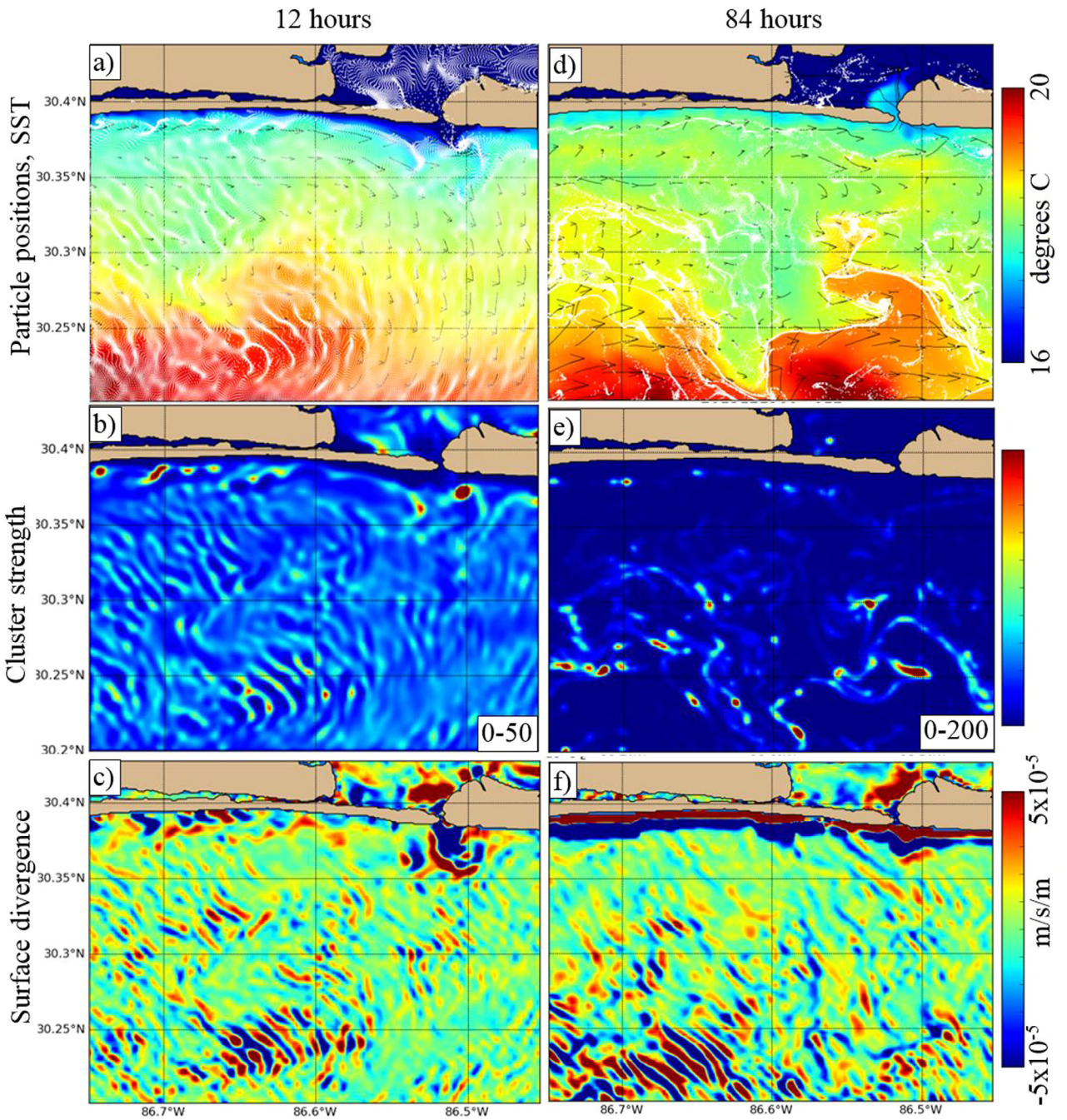

Figure 2. Lagrangian particles initialized on 16 December 2013, 00 GMT, in a uniform distribution in a 250 m resolution ocean model surface flow provide an example of clustering. After 12 h, the particle positions, plotted on top of the model sea surface temperature as white dots, indicate (a) clustering, which is quantified by the (b) cluster strength function, and this is compared to the (c) surface divergence field. Three days later, at 84 h, the (d) particle evolution continues, and the (f) cluster strength increases further. The colorbar range for Figures 2b and 2e is noted in the lower right of each plot. Note the range difference between Figures 2b and 2e. The instantaneous divergence field at 84 h (Figure 2f) is not as well aligned with the cluster strength function as at 12 h.

simultaneous surface divergence field (Figure 2c) displays areas of large amplitude divergence in locations of high and low cluster strength.

After an additional 3 days (Figure 2d), at 84 h, continued clustering is observed as the cluster strength function (Figure 2e) increases amplitudes beyond that at 12 h. However, ridges in the instantaneous divergence field at 84 h (Figure 2f) do not clearly align with features in the cluster strength field. Though divergence

drives clustering, the relation between divergence and clustering is more complicated, and the cumulative effect of divergence is best explored from the Lagrangian perspective. As will be shown, this approach leads to a closed form expression relating the Lagrangian divergence (LD) time series to clustering evolution.

Clustering at the ocean surface can be characterized by dilation, which is the ratio of deformed material element area to the original area [*Huntley et al*., 2015]. In the absence of diffusion and other sources or sinks, as the area of a material element changes, the number of particles or quantity of substance within it remains constant. Thus, as a measure of change in material area, dilation is a quantification of change in density, which is clustering.

Area changes have been estimated by tracking triads of particles in numerical models [*Kalda et al*., 2014]. Finite separation between particles in areas of large shear such as around the Loop Current Eddy (LCE) and integration over long time can lead to large errors in the estimate. Therefore, we choose a method of directly integrating the Lagrangian deformation tensor $\boldsymbol{F}_{ij}=\frac{\partial x_i}{\partial X_j}$, with x_i the position of a particle and X_j its initial position, as described by *Huntley et al*. [2015]. The initial condition for **F** is the identity matrix, and **F** is computed by integrating along a particle trajectory:

$$\mathbf{F}(T)=\int_0^T \frac{D\mathbf{F}}{Dt}dt, \tag{2}$$

where $\frac{D}{Dt}$ is the total derivative along a material trajectory. This tensor describes the deformation following a material element along its trajectory, and hence is a Lagrangian property. The time rate of change of **F** is the tensor product of the local velocity gradient and the deformation tensor itself:

$$\frac{D\boldsymbol{F}}{Dt}=(\nabla \boldsymbol{v})^{\boldsymbol{T}}\mathbf{F}. \tag{3}$$

The total material deformation in two dimensions can be decomposed into three components: rotation, dilation (area change), and stretch (elongation along one axis and compensating contraction in the perpendicular direction without area change). Rotation is not of significant interest for our purposes. Dilation and stretch can be recovered from the singular value decomposition of **F**. Let $\mu_1 \geq \mu_2$ be the two singular values of **F**. Then dilation is defined as $\delta=\mu_1\mu_2$, and stretch is $s=\mu_1/\mu_2$. The singular vectors of **F** provide the principle directions of stretch, whereby the leading singular vector corresponds to the direction of elongation.

To understand the relation between LD and dilation or clustering, it is useful to examine the evolution equation of dilation that may be derived from equation (3):

$$\frac{1}{\delta}\frac{D\delta}{Dt}=\nabla\cdot\mathbf{v}(\mathrm{x}(t)), \tag{4}$$

where $\nabla\cdot\mathbf{v}(x(t))$ is the LD, that is, the time series of divergence along the Lagrangian trajectory $x(t)$. Given the time-dependent $\mathrm{LD}(T)$, the closed form solution for equation (4) is

$$\delta=\exp\left(\int_0^T \mathrm{LD}(t)dt\right). \tag{5}$$

If the LD is constant, equation (5) at time T becomes $\delta=\exp((LD)T)$. Constant LD leads to exponentially changing dilation, either increasing or decreasing depending on the sign of LD. Because of this exponential relationship, it is convenient to examine

$$\Delta=\frac{\ln(\delta)}{T}=\frac{1}{T}\int_0^T \mathrm{LD}(t)dt. \tag{6}$$

We refer to this as the average dilation rate (ADR). In the case of constant LD, the ADR is equal to LD. For time-varying $\mathrm{LD}(T)$, the ADR is the time averaged LD. At time T, the dilation is $\delta=\exp((ADR)T)$. The ADR has an additional interpretation: *Huntley et al*. [2015] point out that the widely used finite-time Lyapunov exponent (FTLE) is the average of the ADR and the average stretch rate.

In the initial example, the ADR (Figures 3a and 3c) contains structures similar to the cluster strength (Figures 2b and 2e). The correspondence of cluster strength and dilation is also exhibited in the joint distribution of

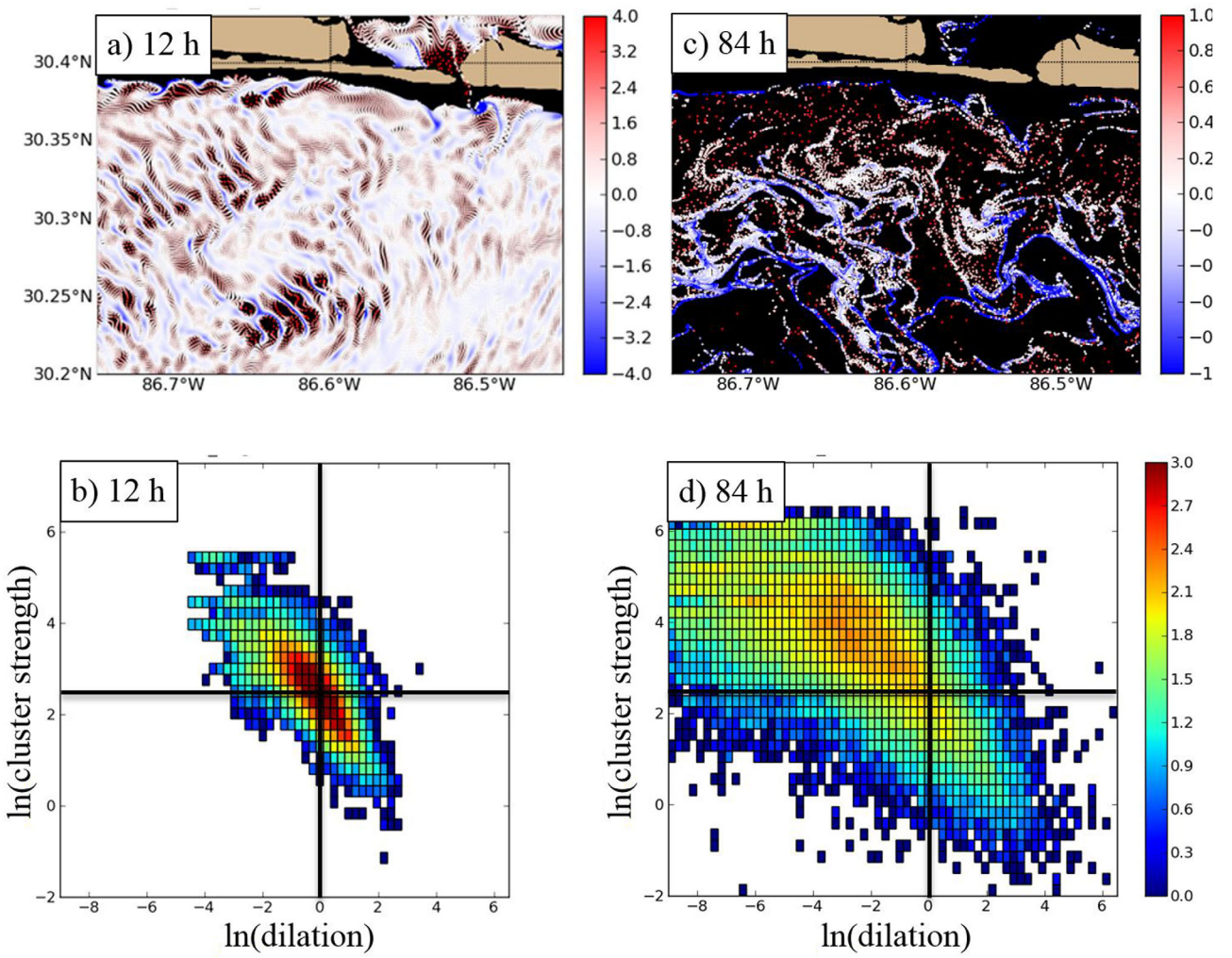

Figure 3. From the 250 m model, at the same times as Figure 2, at 12 h the (a) average dilation rate and (b) PDF of natural log of cluster strength versus dilation. At 84 h, (c) average dilation rate and (d) PDF of natural log of cluster strength versus dilation. Information in Figures 3a and 3c is plotted at particle locations; black areas are void of particles. The colorbar range in Figures 3b and 3d is the log10 of number of samples in each bin. At initial time, ln(dilation) is 0 and ln(cluster strength) is 2.46 for all particles.

the natural logarithms of dilation and cluster strength (Figures 3b and 3d). Note that the initial value of ln(dilation) is 0, and the initial value of ln(cluster strength) is 2.46 for all particles. Locations of high cluster strength correspond to decreased material area indicated by dilation less than 1 and thus negative values of $\ln(\delta)$. The largest scatter occurs for $\ln(\delta) < -4$, where the material is compressed to a very small fraction of its original size. Scatter is due to the limited ability of a finite number of particles to represent continuous material density in computing cluster strength by equation (1).

The cluster strength fields (Figures 2b and 2e) suggest that different physical processes dominate clustering after different evolution times T. Smaller-scale structures are initially apparent with larger-scale structures appearing later. We will see that this is a general result that holds across scales. Different spatial scales are related to different temporal scales through the ocean processes controlling the LD.

To investigate this relationship, consider LD at a particular frequency. Specifically, assume LD is of the form $\mathrm{LD}(t)=d\cos(2\pi t/p)$, where d is a constant amplitude and p is a constant period. Initially, when material is placed on the ocean surface, the evolution time is much less than the period of $\mathrm{LD}(t)$: $T \ll p$. During this initial time, the LD is relatively constant, dilation increases exponentially according to (5) and the ADR is relatively constant according to (6). As the evolution time increases so that $T \gg p$, the LD is oscillating, bounded by peak amplitude d, dilation is oscillating within a fixed bound, and the ADR is continually decreasing as T increases. These relations are summarized in Table 1.

Table 1. The Characteristics of Dilation and ADR Given Sinusoidal LD With Amplitude d and Period p Relative to the Evolution Time T

Evolution Time T Versus LD Period p	Dilation δ	Average Dilation Rate Δ
$T \ll p$	Exponential growth: $\delta \cong \exp(dT)$	$\Delta \cong d$
$T \gg p$	Bounded oscillation: $\exp(-dp/(2\pi)) \leq \delta \leq \exp(+dp/(2\pi))$	$-dp/(2\pi T) \leq \Delta \leq dp/(2\pi T)$

Now consider two processes with divergence amplitudes $d_1 > d_2$ and periods $p_1 < p_2$, where a smaller-scale process has larger amplitude divergence and a shorter Lagrangian period. When $T \ll p_1$, the dilation contribution of both processes increases exponentially, and the ADR of each is relatively constant. During this time, since $d_1 > d_2$, the effects of the shorter period process on dilation are initially more apparent. When $p_1 \ll T \ll p_2$, the dilation due to the first process becomes bounded, with decreasing ADR, while the dilation due to the second process continues exponential growth, with near-constant ADR.

This explains the results in the ADR of Figures 3a and 3c. The shorter time period dilation effects are initially apparent at 12 h (Figures 2a, 2b, and 3a). These effects become bounded in amplitude, and the longer period effects continue to grow exponentially leaving the long period effects more apparent at 84 h (Figures 2d, 2e, and 3b).

3. The Model Hierarchy

Ocean processes produce divergence across the spectrum of time scales with short time scales typically associated with shorter spatial scales and stronger divergence. The approach for separating these ocean processes is through limiting resolution of numerical ocean models. At a given resolution, a numerical second-order-accurate finite difference scheme represents derivatives accurately if the wavelengths are longer than 8–10 grid points. Within the ocean models used here, at every time step, an Asselin filter [*Asselin*, 1972] actively damps features at scales of twice the grid spacing. Therefore, a grid of specified resolution will necessarily limit the scales of physical processes a model may represent. As grid resolution is increased, additional processes become resolved. We take advantage of this to add processes incrementally by increasing resolution.

The numerical model is the Navy Coastal Ocean Model (NCOM) [*Barron et al.*, 2006]. The outer domain for the experiments (Figure 4) covers the entire GoM with both 3 and 1 km horizontal resolution model setups. Inside the 1 km setup is nested a 250 m model, and within this a 50 m resolution model is implemented. The outer domain is forced by boundary conditions from the operational global HYCOM. For all setups, the vertical grid uses 16 z levels below 34 sigma levels for a total of 50 levels. Sigma levels cover the upper 550 m of the water column. The thinnest layer at the surface has a thickness of 0.5 m, and deeper layers telescope to the thickest sigma layer of 85 m centered at a depth of 510 m. The high vertical resolution near the surface is intended to permit submesoscale physics. All model experiments are forced by the same atmospheric conditions from the Coupled Ocean/Atmosphere Mesoscale Prediction System, COAMPS [*Hodur*, 1997]. The surface wind stress is determined from the atmospheric model 10 m wind velocity. Bulk flux formulations provide surface heat fluxes using the 10 m air-temperature and humidity, along with the ocean model sea surface temperature (SST). Tidal potential forcing is applied to the interior of the domain, and tidal boundary conditions for water level and barotropic velocity are provided by the Oregon State University global Ocean Tide Inverse Solution (OTIS) [*Egbert and Erofeeva*, 2002] at the domain boundaries. Thus, locally generated tides are present in the model. Observations from satellite and in situ sources are assimilated into the 3 and 1 km experiments [*Jacobs et al.*, 2014] but not the 250 or 50 m ones.

Both the 3 and 1 km experiments are initialized on 1 May 2012, and the window of 20 July 2012 to 30 August 2012 is used for the analysis here. The 250 m domain covers the area 29.04°N–30.44°N, 87.36°W–85.82°W (Figure 4). The 50 m domain covers the area 30.27°N–30.39°N, 86.60°W–86.52°W. The 250 m domain is initialized from the 1 km model on 1 October 2013, and the 50 m domain is initialized from the 250 m domain on 1 November 2013. Results from the nested systems are examined starting 16 December 2013. This provides sufficient time for initial condition transients to damp in the deep water mesoscale field and for higher-resolution local dynamical processes to reach equilibrium.

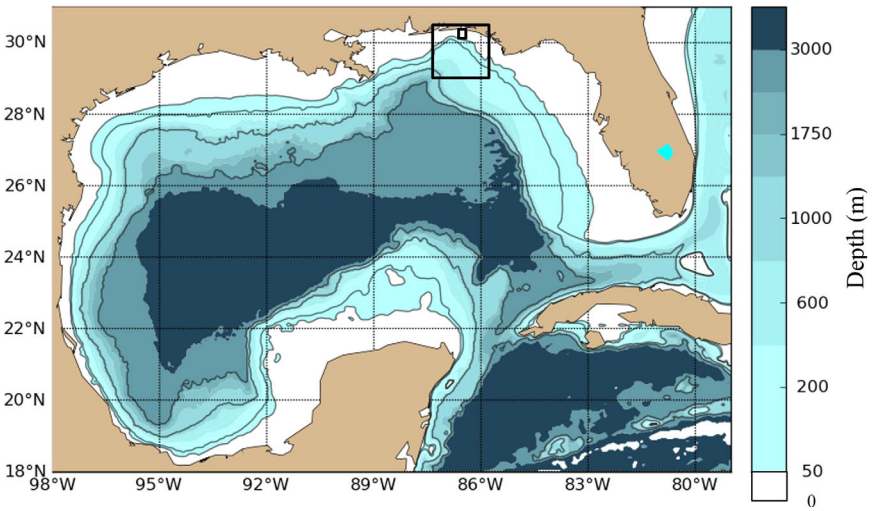

Figure 4. The domain and bathymetry used for the 3 km resolution and 1 km resolution experiments cover the entire Gulf of Mexico. The larger black box in the northeastern Gulf of Mexico is the domain covered by the 250 m resolution nest. The very small box inside the 250 m domain indicates the 50 m nest.

4. Resolved Ocean Processes and Their Divergence Properties

The main mesoscale processes in the northeastern GoM in July to September 2012 are the LCE and associated shingle cyclones. The GLAD experiment observed the eddy evolution by deploying 295 CODE-style drifters during 22–30 July 2012, in this area, and verified that the 3 km resolution ocean model captures the main synoptic mesoscale features [*Jacobs et al*., 2014]. The mesoscale field at scales greater than 100 km is primarily geostrophically balanced. This mesoscale flow described by the sea surface height and geostrophically balanced currents produces zero surface divergence and no clustering [*Huntley et al*., 2015]. Large-scale atmospheric drag interacts with mesoscale ocean eddies to produce differential stress relative to the water velocity on one side of a mesoscale eddy versus the other. The resulting spatially varying Ekman transport across the eddy results in upwelling and thus divergence [*McGillicuddy et al*., 2007]. However, the resulting divergence is relatively small. Submesoscale processes at scales of tens of km have much stronger associated vertical flow and thus surface horizontal divergence [*Thomas and Ferrari*, 2008]. Such processes have been observed by instrumented ocean gliders in the northwest Mediterranean [*Niewiadomska et al*., 2008] and by shipboard surveys in the Sargasso Sea [*Shcherbina et al*., 2013]. *Pollard and Regier* [1992] diagnose the vertical velocity field from temperature and salinity observations through the omega equation, and *Mensa et al*. [2013] provide an overview of modeled submesoscale dynamics in frontogenesis and mixed-layer instabilities.

In the 3 km model, frontogenesis is the primary mechanism producing ageostrophic flow. The frontogenesis forcing is the confluence of water masses of different buoyancies. Because the geostrophically balanced mesoscale flow drives the velocity and buoyancy fields, the areas of frontal formation appear as bands around the mesoscale features. Confluence occurs in areas around the edges of the mesoscale field associated with high-vorticity bands (Figure 5a). Frontogenesis forcing is described by the omega vector or $Q1$ [*Hoskins*, 1982; *Mensa et al*., 2013; *Pollard and Regier*, 1992], which is the total derivative of the horizontal buoyancy gradient:

$$Q1 = \left(\frac{D_g}{Dt} b_x, \frac{D_g}{Dt} b_y\right) = \left(-u_{gx} b_x - v_{gx} b_{y,} - u_{gy} b_x - v_{gy} b_{y,}\right), \tag{7}$$

where D_g/Dt is the total derivative using the geostrophic velocity, and (b_x, b_y) is the gradient of the buoyancy field. The frontogenesis forcing $Q1$ (magnitude shown in Figure 5b) drives vertical circulation and generates associated divergence (Figure 5c).

At 1 km resolution, relative to the 3 km results, the surface vorticity exhibits additional small-scale intense features (Figures 5a and 5d). These features are strong within the mixed layer, and the small-scale relative vorticity at the surface (Figure 5d) decreases substantially below the mixed-layer depth at about 50 m (not

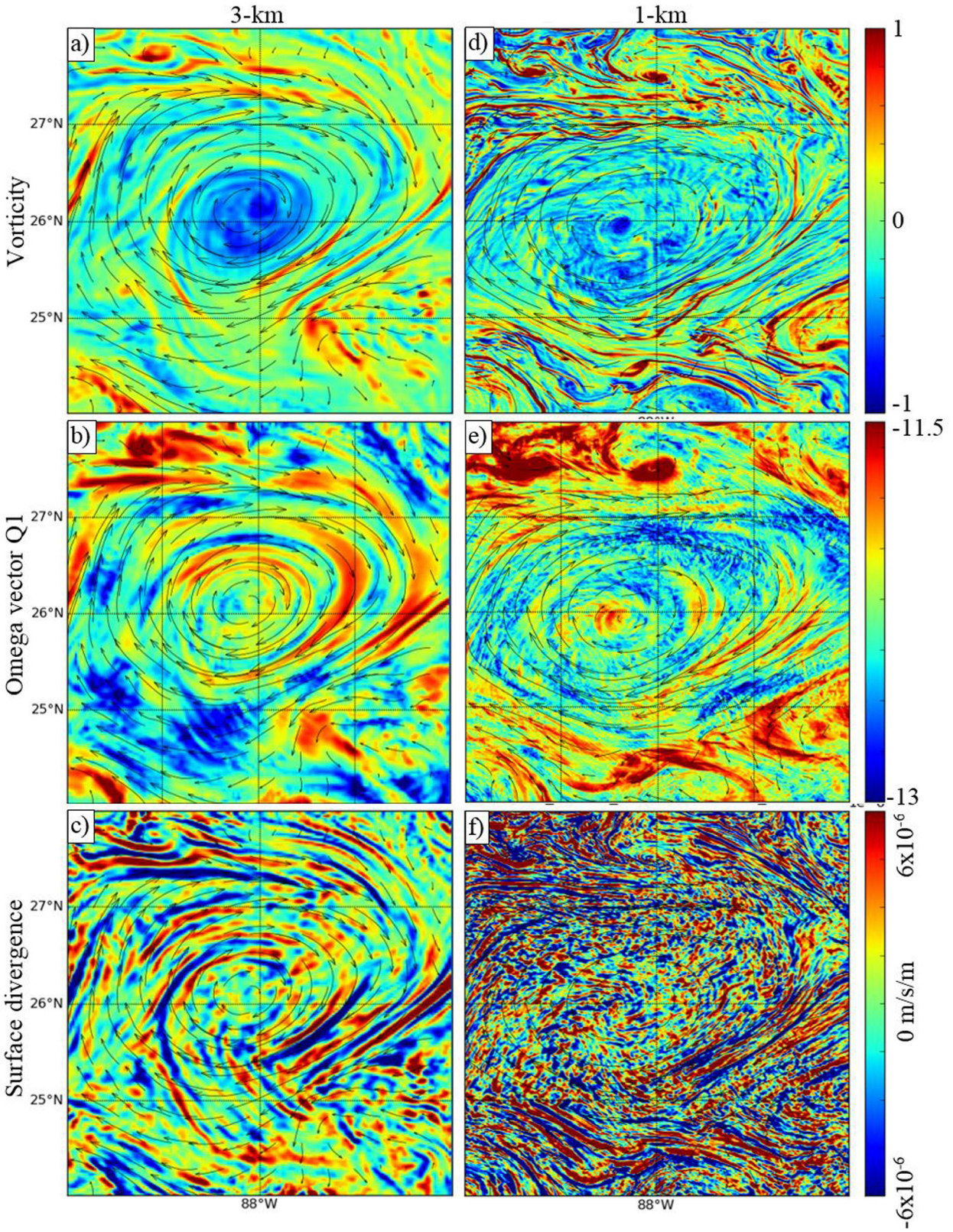

Figure 5. The 6 August 2012 (top) surface vorticity normalized by Coriolis parameter, (middle) log10 of frontogenesis forcing *Q*1, and (bottom) surface divergence from (left) the 3 km model and (right) the 1 km model.

shown). Thus, this phenomenon can be ascribed to submesoscale mixed-layer instabilities with scales on the order of 10 km that are represented at 1 km resolution but not at coarser resolution [*Capet et al*., 2008]. Submesoscale mixed-layer instabilities have been shown to produce clustering in idealized situations [*Zhong and Bracco*, 2013].

Both the 3 and 1 km resolution systems contain the LCE at approximately the same location, since both are assimilating the same observations. Some variation in the position of the LCE front is due to observational data limitations. Since the positioning of the frontogenesis forcing is very sensitive to slight position changes in the LCE and surrounding eddies, it is not expected that the $Q1$ forcing bands align spatially between the models (Figures 5b and 5e). On the other hand, the spatial scales and amplitudes are quite comparable.

A comparison of the frontogenesis forcing $Q1$ (Figures 5b and 5e) shows the mesoscale eddy-driven frontogenesis bands are slightly more intense at 1 km resolution, while the spatial scales are similar. Prior studies have shown that 3 km is the point at which numerical systems converge to accurately represent the mesoscale physics [*Hogan and Hurlburt*, 2000; *Hurlburt and Hogan*, 2000]. Since the frontogenesis forcing mechanism is a confluence of buoyancy masses, and the bands in the 3 km model are driven by the mesoscale field, increasing resolution to 1 km does not significantly change the mesoscale-driven frontogenesis. The 1 km resolution can represent increased gradients across fronts, and thus the 1 km model can have slightly stronger $Q1$. The $Q1$ at 1 km resolution contains substantially more smaller-scale features associated with the submesoscale mixed-layer instabilities. Comparison of surface divergence in the 3 and 1 km models (Figures 5c and 5f) indicates the impact of mixed-layer instabilities, resulting in much stronger small-scale surface divergence at 1 km resolution.

The two nested model experiments with 250 and 50 m resolutions represent additional processes. In the deep ocean, south of the shelf break, the general circulation eddy features are similar between the 1 km and 250 m results (Figure 6). A cyclonic and anticyclonic eddy pair extends through the southern boundary of Figure 6. The location of particular divergence fronts wrapping around mesoscale features is not expected to coincide, though the fronts outline similar mesoscale circulation. Again, the higher-resolution model produces sharper divergence fronts with smaller cross-frontal distance.

Dynamics within shelf break fronts result in strong divergence [*Barth et al*., 1998], and the shelf break front is a prominent process in both the 250 m and 1 km divergence fields (Figure 6). High-energy meanders occur due to the instabilities generated as the deep thermocline and halocline meet the bottom topography between 150 and 200 m depth. The instabilities extend onto the shelf to the 50 m isobaths and beyond in some cases. The shelf break front meanders in the two models are also not expected to coincide, as the features are instabilities not constrained by observations.

The 250 m model shows markedly increased divergence amplitude on the continental shelf, where it begins to resolve the bathymetry features and thus interactions that the 1 km model cannot resolve. Bottom boundary layer effects on the continental shelf give rise to localized upwelling and downwelling connected to bathymetric features [*Kurapov et al*., 2005]. To aid in visualizing the relations, the local troughs and ridges of the model bathymetry are identified in black and white and shown over the bathymetry in color (Figures 7a and 7d). The currents in the bottom sigma layer of the model provide the estimate of bottom divergence. Convergence occurs on the lee side of ridges, which is seen in the model when the flow is westward as blue areas to the west of the white ridges (Figures 7b and 7e). Divergence occurs on the east side of ridges, which is seen by the red areas west of the black troughs. The spatial scales of divergence on the shelf reflect the spatial scales of bathymetry, which cover a broad range. The bathymetrically controlled divergence is stronger at smaller scales. Thus, the bathymetry features produce intensified divergence with 50 m resolution versus 250 m resolution (Figures 7b and 7e).

The results are consistent with topographically generated internal waves [*Gill*, 1982]. Such interactions with flow over topography have been studied extensively in the atmosphere. The convergence on the lee side of ridges results in vertical motions and rain bands that are orographically fixed [*Anquetin et al*., 2003]. One substantial difference lies in the ocean's vertical boundaries. In the atmosphere, bottom vertical velocity has a substantial distance to travel. Ocean vertical velocity, generated by the bottom divergence on the continental shelf, meets the ocean surface, which imposes another kinematic boundary condition. The result is surface divergence in the ocean, which is of the opposite sign as the bottom divergence. This is shown in

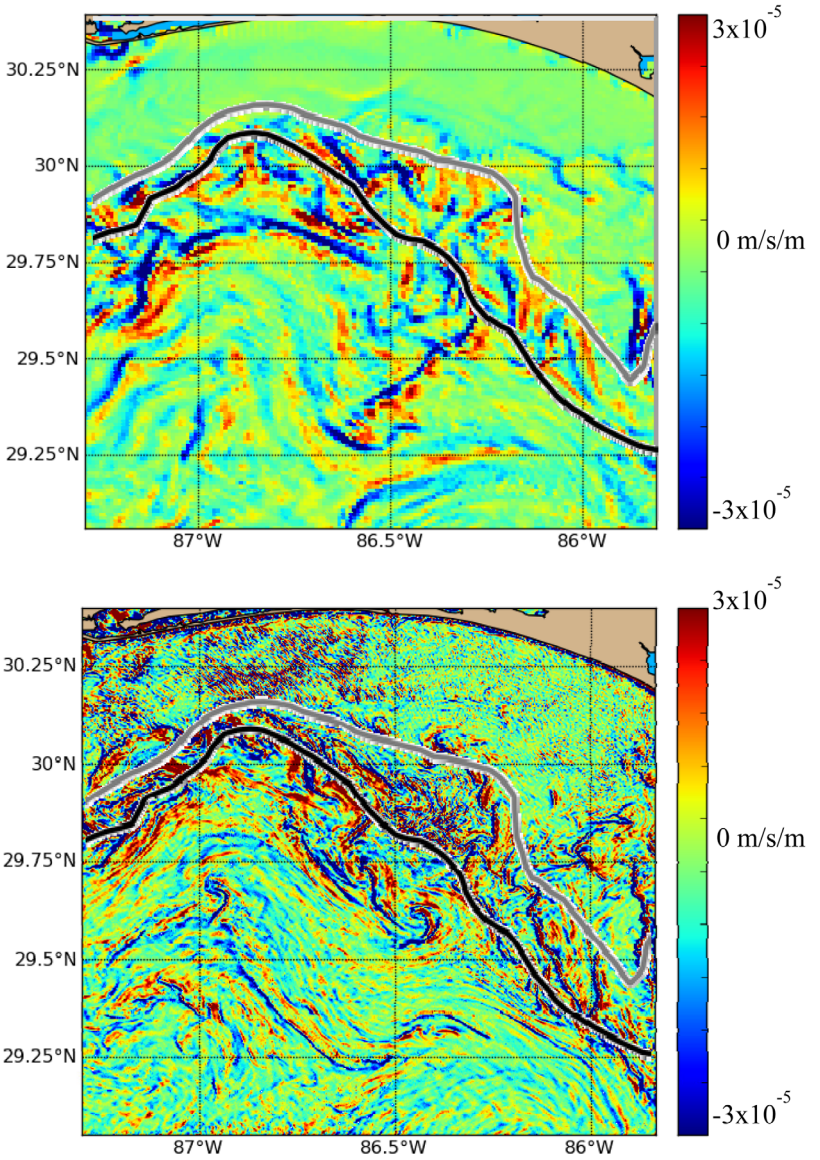

Figure 6. Comparison of (top) 1 km and (bottom) 250 m surface divergence on 16 December 2013, over the northeastern GoM. The thick black and grey lines denote the 100 and 50 m isobaths, respectively.

the joint distribution of bottom and surface divergence for both the 250 and 50 m models (Figures 7c and 7f) as a negative correlation between the divergence in the model surface and bottom sigma layers. Thus, the bathymetry structure appears in the surface divergence as well. The surface divergence features of scales of about 2 km in the initial example (Figure 2c) are associated with bathymetry and hence retain their character 3 days later (Figure 2f). The bathymetry-associated divergence produces the initial clustering pattern of surface particles (Figure 2a).

Note that the time period examined on the continental shelf, 12–18 December 2013, was characterized by relatively calm winds. Thus, topographic interactions are more dominant and more easily identified. We do not intend to imply that the bathymetric relation to divergence is the dominant process at all times. Certainly, wind forcing can cause substantial surface divergence, and we do not provide a complete cataloging of all ocean processes.

As model resolution is incrementally increased, additional ocean processes contribute to the surface divergence structure. The mesoscale and submesoscale-driven frontogenesis, shelf break front, and

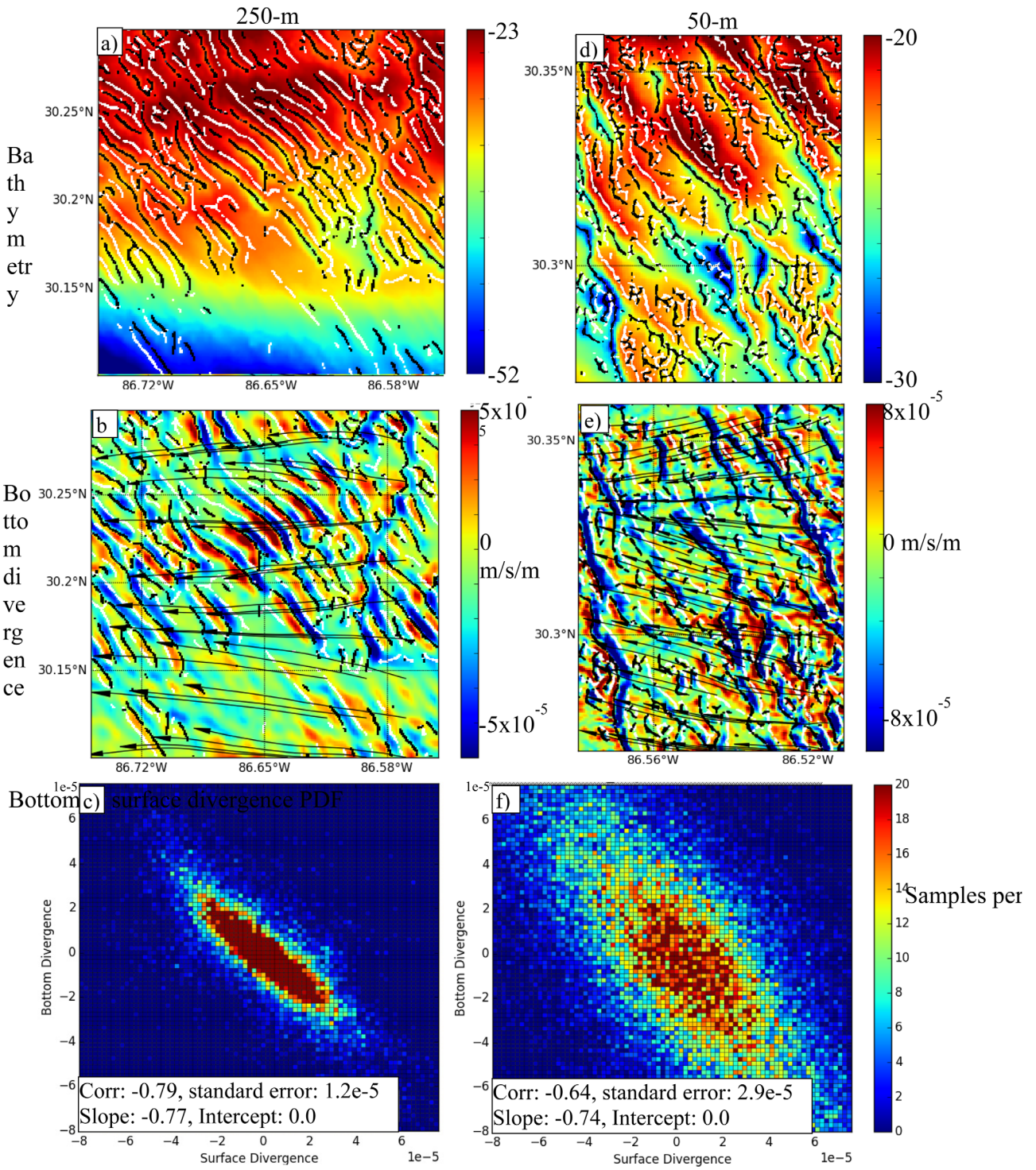

Figure 7. (top) Bathymetry, (middle) bottom currents and divergence, and (bottom) the joint distribution of bottom and surface divergence on 15 December 2013, 00 GMT for subdomains of the (left) 250 m and (right) 50 m experiments. Note the difference in color bar ranges for depth and divergence. Positions of bathymetric troughs (black) and ridges (white) are outlined on the bathymetry and divergence.

bathymetrically controlled processes each contribute to the instantaneous Eulerian divergence fields in Figures 5–7. However, to draw the connection to clustering, we must consider how each of the added processes changes the LD and its spectrum.

5. Ocean Process LD Spectrum and Clustering

For a more in-depth analysis of the LD spectrum, we first consider the period from 20 July 2012 to 30 August 2012, for the 1 and 3 km models. The initial particle positions on 20 July for both experiments cover the entire GoM domain at 1 km spacing. The LD power spectral densities averaged over all particles (Figure 8, top) contain high energies at the low frequencies and local peaks in the vicinity of 1 cycle per day (cpd). The power spectral density is averaged over the low-frequency (0.0–0.2 cpd) and daily (0.8–1.2 cpd) bands and displayed at the particle initial position to provide the spatial distribution of LD power density.

Both the low-frequency and 1 cpd bands in the 3 km results (Figure 8) contain filaments of high LD spectral energy wrapping around the LCE centered near 88°W 26°N. At the low frequencies, these high-energy bands are the result of the frontogenesis around the eddy. Because of the mesoscale confluence along the front driving the frontogenesis divergence, a particle initially in a frontogenesis band will spend a long time in the same divergence field. Thus, mesoscale-driven frontogenesis contributes to the low-frequency LD spectral energy. Prior spectral examinations of the 3 km and drifter observations from the 2012 GLAD experiment [*Jacobs et al*., 2014] indicate high spectral energy in the clockwise rotating spectrum near the inertial frequency with high coherence between model and observations. The 1 cpd energy around the LCE periphery is possibly an interaction of inertial oscillations with the frontal currents. In the higher-resolution 1 km results, mixed-layer instabilities increase LD energy at all frequencies. These added processes increase the low frequency and daily energy especially outside the LCE core and along the shelf break, where freshwaters from the Mississippi River create strong buoyancy gradients with the more saline deep waters.

To compare the 250 m and 1 km results, the particles are initially spaced 100 m apart in both models and advected from 12 December 2013 to 18 December 2013. Analysis of the LD spectrum is conducted over the area in Figure 9, which includes both the shelf break front and the shelf areas. From 1 km to 250 m resolution, the spectral energy content increases at all frequencies with larger increases at higher frequencies. Because of this, we also include the spatial distribution of LD spectral energy density at high frequency (3–4 cpd) in the analysis.

Across the shelf region, the 1 km LD contains relatively low energy levels in the low-frequency and daily bands, and very little energy in the high-frequency band. The 250 m LD contains significant energy at all frequency bands across the shelf (Figure 9). This is consistent with the Eulerian divergence snapshot in Figure 6 in that stronger divergence amplitudes exist on the continental shelf due to greater bathymetry resolution and associated interactions. The bathymetric features in Figure 7 have scales of about 2 km wavelength, which are not resolved in the 1 km resolution model. Across the shelf break front, the 1 km LD contains high energy in the low frequency with little energy at higher-frequency bands (Figure 9). The 250 m LD shows increased energy across the shelf break front throughout all frequency bands.

As discussed in section 2 and summarized in Table 1, the LD and its spectrum can explain clustering evolution. Once material is placed on the ocean surface, the most prominent clustering features are the result of the strongest divergence. The divergence snapshots in Figures 5–7 indicate stronger divergence at smaller spatial scales, which implies that the corresponding processes will dominate the early clustering evolution. On the shelf, the small-scale and short LD period processes are primarily topographically controlled currents, while in the deep ocean these are mixed-layer instabilities. Over time, the ADR effects diminish for processes with periods less than the evolution time. Processes acting on longer time scales—the shelf break front and frontogenesis along the LCE edge—support a more constant ADR and become the predominant features in clustering patterns.

Dilation and ADR are properties associated with a particle's entire trajectory, but for visualization purposes, a unique location must be chosen. The two natural choices are either the initial or final position of each particle. Both have advantages and disadvantages. Using the initial position enables the viewer to follow the evolution of dilation for an individual particle since a given location is continually identified with the same material particle. The use of final positions lets the viewer identify final particle locations after undergoing the identified dilation. This is particularly useful for relating dilation to clustering (e.g., Figures 3a and 3c). However, viewing information at the final positions leaves large gaps in the fields as well as locations of very dense information hindering interpretation. Thus, the results here are presented at the particle initial positions. Nonetheless, in the relatively small 50 m resolution domain, gaps in spatial coverage appear in Figure 10, since particles leave the domain within the respective analysis periods.

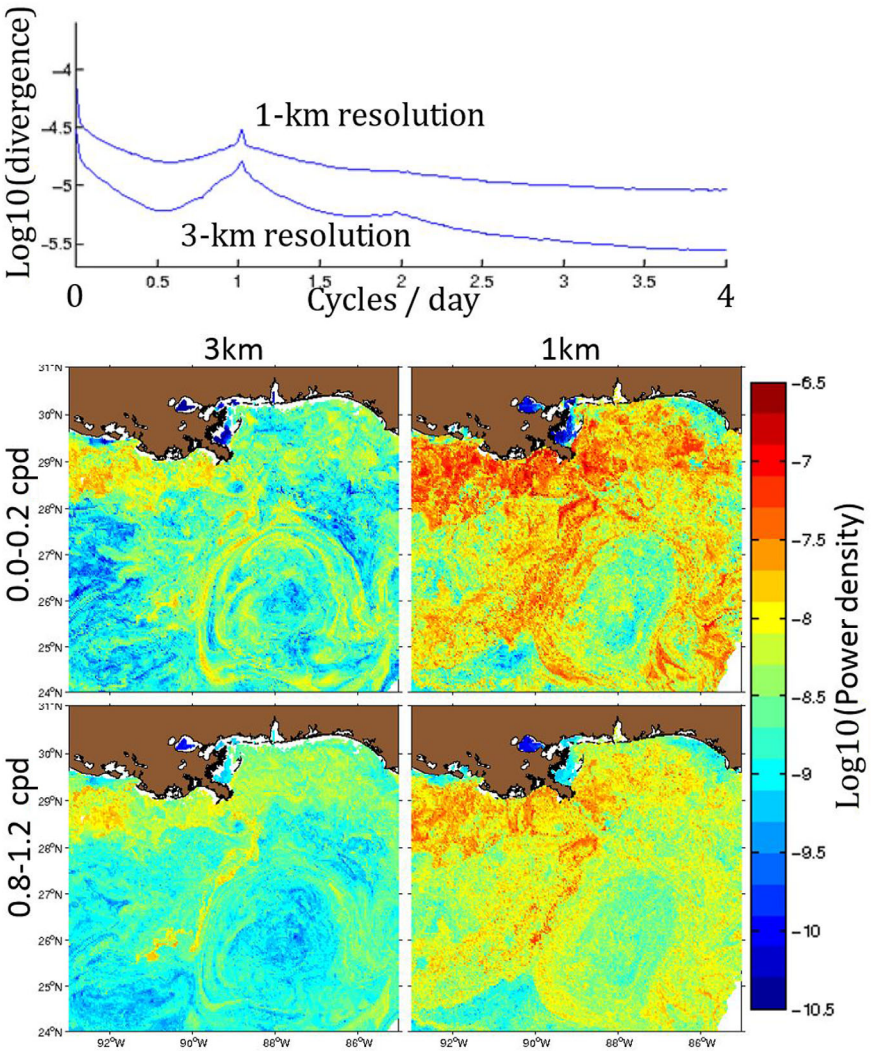

Figure 8. Lagrangian divergence amplitude spectra 20 July 2012 to 30 August 2012, (top) for the 3 and 1 km resolution models indicate local peaks. The energy density averaged over the (middle) low-frequency and (bottom) 1 cpd bands provide the spatial distribution of LD energy.

Three hours after initialization, regions of significant deformation can be identified in the ADR field for the coastal domains of the 50 m and the 250 m resolution models (Figures 10a and 10d). The geographic patterns of low ADR (blue; clusters) and high ADR (red; voids) reflect the spatial scales and locations of the bathymetric features and topographically induced instantaneous divergence field as discussed earlier. With higher bathymetry resolution in the 50 m model, the 3 h ADR field also shows finer features (Figure 10d). Note also that the 50 m model ADR amplitudes are much greater than for the 250 m model (Figure 10a). Since the bathymetry is not changing, with spatial scales of about 2 km in the coastal domain, and typical current speeds in this area are 0.02 m/s, the associated LD period is roughly 24 h. And indeed, at 24 h, the bathymetric signal starts diminishing in the ADR fields (Figures 10b and 10e) implying that particle clusters are no longer as well aligned with the topography. In the 50 m resolution model, interactions with the bathymetry are the main driver of surface divergence.

In the 250 m resolution model, larger spatial scales, associated with longer time scales, become more prominent in the ADR at later times. The shelf break instabilities extend northward to the 50 m isobath (Figure 6) and intrude into the southwest portion of the 250 m resolution domain displayed in Figure 10. Thus, the shelf break front is a dominant feature in the ADR field after both 24 and 72 h (Figures 10b and 10c) with the bathymetrically controlled ADR diminishing in relative importance.

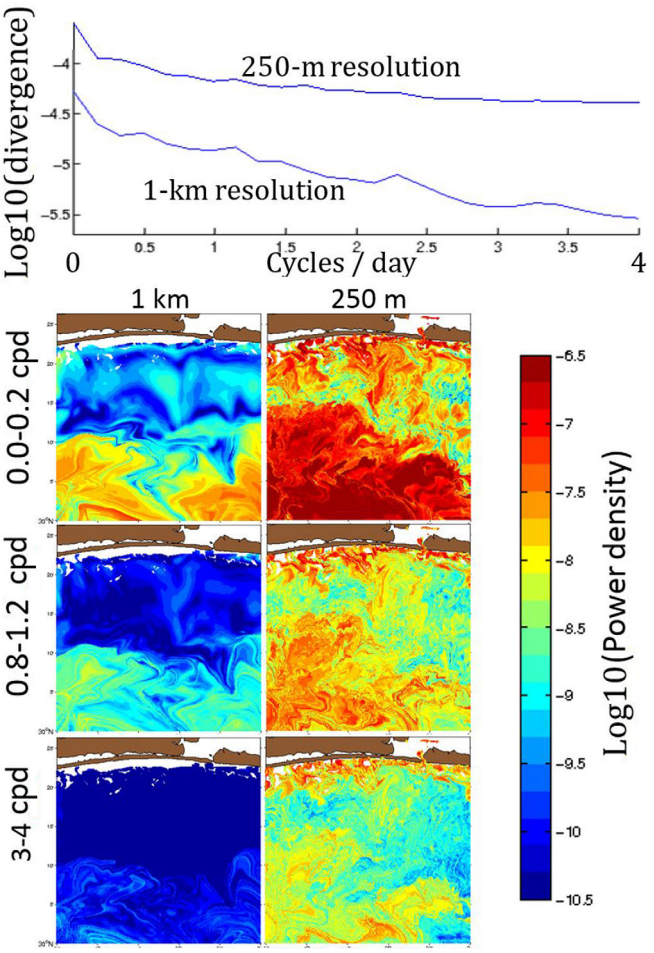

Figure 9. Lagrangian divergence amplitude spectra 12–18 December 2013, (top) for the 1 km and 250 m resolution models indicate local peaks in the 1 cpd band and in the low-frequency band. The energy density averaged over the (second row) low-frequency, (third row) 1 cpd, and (bottom) high-frequency bands provide the spatial distribution of LD energy.

Over the deep ocean, clustering is initially driven by mixed-layer instabilities around the LCE as seen in the 1 km solution (Figure 11a). After 6 h of integration, features with 10 km spatial scales are ubiquitous in the ADR. As these are associated with relatively short LD periods, their importance has diminished in the 72 h frame (Figure 11c), while ADR features controlled by mesoscale frontogenesis filaments wrapping around the LCE, which have longer LD periods (Figure 8), have grown and become predominant. Over longer time periods, the frontogenesis effects diminish even in the 3 km resolution results. The amplitude of the ADR associated with the frontogenesis filaments and thus total ADR amplitude decreases, progressing from 3 to 10 to 24 days (Figures 11d–11f).

While ADR amplitudes associated with a process diminish as integration time extends beyond the LD time period of the process, dilation evolution continues as an oscillation within *constant* bounds (Table 1). This suggests that after an initial exponential growth in density, clusters continue to evolve, undergoing alternating expansion and compression. Clusters form, dissipate, and then recompress with material moving possibly into different clusters.

Although small-scale processes are generally associated with short time periods, the low-frequency LD spectral energy increases as the model resolution increases (Figures 8 and 9). The implication is that stronger clustering, with higher ADR, is present in higher-resolution models at all time scales. The higher-resolution increases the strength of frontal processes and the strength of LD, as in the case of frontogenesis comparisons between the 3 and 1 km experiments. The transition from 1 km to 250 m resolution contains a similar contribution of newly represented small-scale processes on the continental shelf to the low-frequency LD energy. Thus, the effect of increasing resolution and representing small-scale processes also increases clustering at long periods.

6. Summary and Conclusions

Clustering occurs as the density of material on the ocean surface increases over time and can be quantified by dilation, which in turn is governed by the Lagrangian divergence (LD). In the experiments examined, the main processes affecting LD include mesoscale frontogenesis, frontogenesis driven by submesoscale instabilities, the shelf break front instabilities, and bathymetric interactions. Smaller-scale processes contribute stronger surface divergence.

Material placed on the ocean surface experiences initial exponential clustering due to LD generated by all processes. Small-scale processes generating high-frequency LD initially dominate clustering as these have stronger divergence. Therefore, small-scale clustering is dominant until the evolution time exceeds the LD period associated with the small scale, after which these processes contribute to dilation within a bounded

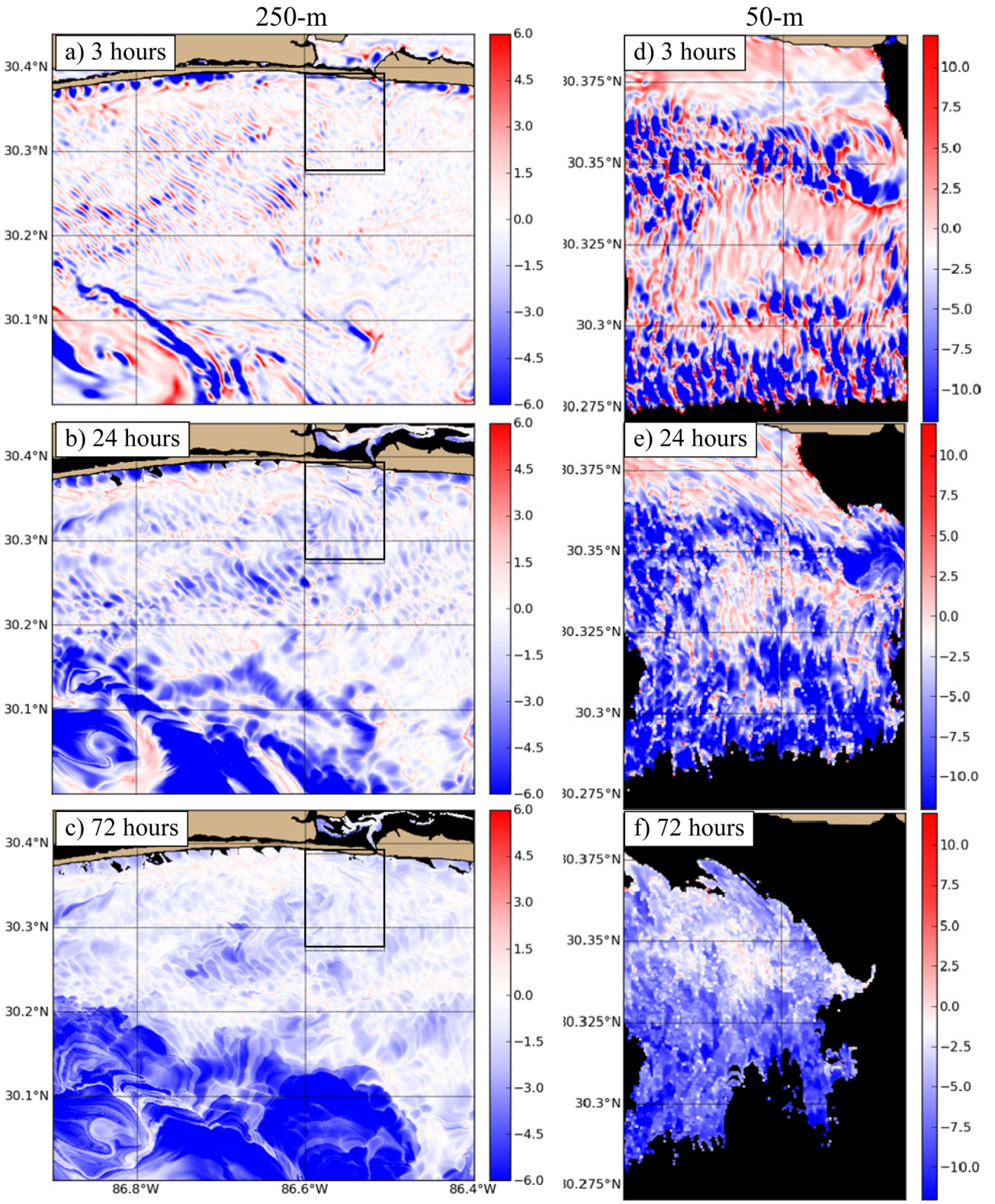

Figure 10. The average dilation rate from the (left) 250 m and (right) 50 m experiments using particles initialized on 12 December 2013. Note the different color bar ranges. As time increases, the ADR decreases for short time period contribution to LD. The initial bathymetry-controlled divergence across the shelf decreases in prominence while the shelf break instabilities increase. The black areas are due to particles leaving the domain. The black box in the left figures indicates the domain of the 50 m results in the right figures.

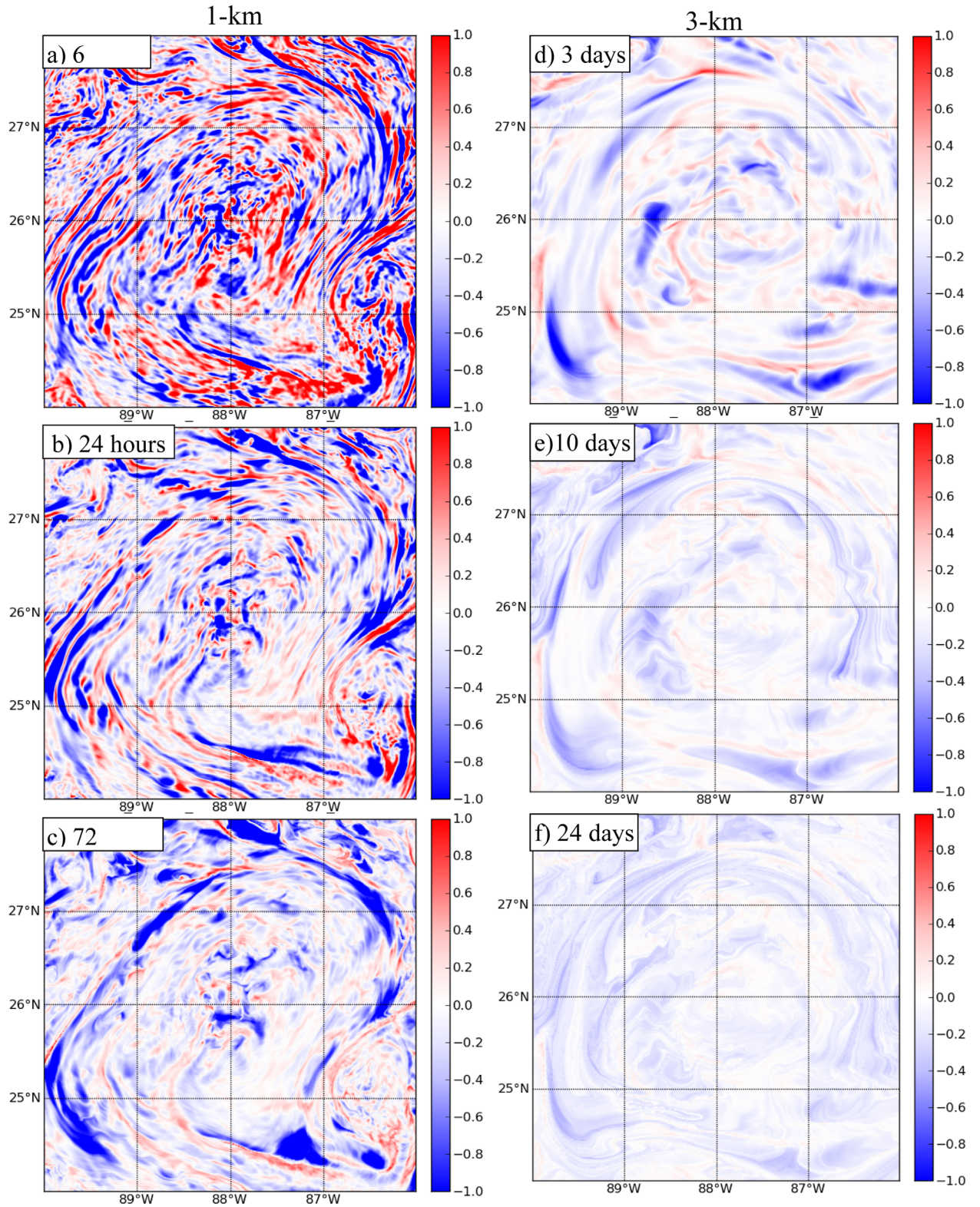

Figure 11. The average dilation rate from the (left) 1 km and (right) 3 km experiments with particles initialized 20 July 2012. Note that the figures cover different time periods. In the 1 km results, the effects of submesoscale mixed-layer instabilities decrease after a few days, leaving the frontogenesis effects. The 3 km results show frontogenesis effects decrease after many days.

range. Lower-frequency LD continues exponential clustering, and this is typically associated with larger spatial scale processes. Thus, the larger scales become more apparent as the clusters evolve. For example, the small-scale topographically controlled clustering yields over time to clustering due to the shelf break front, and the deep water submesoscale clustering yields to mesoscale frontogenesis clustering.

As finer scale processes are resolved, the LD increases across the spectrum. The high-frequency (1 cpd and greater) LD spectral energy increases significantly as topographic interactions are resolved on the continental shelf. The LD spectral energy at low frequencies increases as well with each increase in resolution, indicating that small-scale processes possibly provide a mechanism to alter particle trajectories that heighten the effectiveness of larger-scale longer-period clustering processes. Though not examined specifically here, the localized peaks near 1 cpd in the LD spectra indicate the possibility of inertial oscillation interactions.

The underlying ocean processes along with an understanding of clustering development over time provide a starting point from which we can understand the evolution of the density of passive material on the ocean surface. Clustering is an observed effect across the ocean at many scales. Many substances on the ocean surface experience density changes due to their own particular processes, but the ocean transport contribution to the material deformation is significant in determining material distribution.

Acknowledgments

This research is funded by a grant from BP/The Gulf of Mexico Research Initiative to the Consortium for Advanced Research on the Transport of Hydrocarbon in the Environment (CARTHE). The authors would like to acknowledge the discussions and considerations of the entire CARTHE research group throughout the development of this work including Tamay Özgökmen, Andrew Poje, Javier Francisco Beron-Vera, Angelique Haza, Josefina Olascoaga, Annalisa Griffa, William Dewar, and many others. This paper is contribution NRL/JA/7320—11-1001and has been approved for public release. Data from model experiments may be obtained through the Gulf of Mexico Research Initiative archival site at https://data.gulfresearchinitiative.org under DOI numbers: 10.7266/N7FQ9TJ6, 10.7266/N76Q1V5G, 10.7266/N72Z13F4, or by contacting the first author.

References

Anquetin, S., F. Minsicloux, J. D. Creutin, and S. Cosma (2003), Numerical simulation of orographic rainbands, *J. Geophys. Res.*, *108*(D8), 8386, doi:10.1029/2002JD001593.

Asselin, R. (1972), Frequency filter for time integrations, *Mon. Weather Rev.*, *100*(6), 487–490.

Barron, C. N., A. B. Kara, P. J. Martin, R. C. Rhodes, and L. F. Smedstad (2006), Formulation, implementation and examination of vertical coordinate choices in the Global Navy Coastal Ocean Model (NCOM), *Ocean Model.*, *11*(3-4), 347–375.

Barth, J. A., D. Bogucki, S. D. Pierce, and P. M. Kosro (1998), Secondary circulation associated with a shelfbreak front, *Geophys. Res. Lett.*, *25*(15), 2761–2764.

Capet, X., J. C. McWilliams, M. J. Molemaker, and A. F. Shchepetkin (2008), Mesoscale to submesoscale transition in the California current system. Part II: Frontal processes, *J. Phys. Oceanogr.*, *38*(1), 44–64, doi:10.1175/2007JPO3672.1.

Egbert, G. D., and S. Y. Erofeeva (2002), Efficient inverse Modeling of barotropic ocean tides, *J. Atmos. Oceanic Technol.*, *19*(2), 183–204.

Gill, A. E. (1982), *Atmosphere-Ocean Dynamics*, vol. xv, 662 pp., Academic Press, N. Y.

Gower, J., C. M. Hu, G. Borstad, and S. King (2006), Ocean color satellites show extensive lines of floating sargassum in the Gulf of Mexico, *IEEE Trans. Geosci. Remote Sens.*, *44*(12), 3619–3625.

Handler, R. A., R. P. Mied, T. E. Evans, and T. F. Donato (2001), Convergence fronts in tidally forced rotating estuaries, *J. Geophys. Res.*, *106*(C11), 27,145-27,162.

Hodur, R. M. (1997), The Naval Research Laboratory's coupled ocean/atmosphere mesoscale prediction system (COAMPS), *Mon. Weather Rev.*, *125*(7), 1414–1430.

Hogan, P. J., and H. E. Hurlburt (2000), Impact of upper ocean-topographical coupling and isopycnal outcropping in Japan/East sea models with 1/8 degrees to 1/64 degrees resolution, *J. Phys. Oceanogr.*, *30*(10), 2535–2561.

Hoskins, B. J. (1982), The mathematical theory of frontogenesis, *Annu. Rev. Fluid Mech.*, *14*, 131–151.

Hurlburt, H. E., and P. J. Hogan (2000), Impact of 1/8 degrees to 1/64 degrees resolution on Gulf Stream model—Data comparisons in basin-scale subtropical Atlantic Ocean models, *Dyn. Atmos. Oceans*, *32*(3-4), 283–329.

Jacobs, G. A., B. P. Bartels, D. J. Bogucki, F. J. Beron-Vera, S. S. Chen, E. F. Coelho, M. Curcic, A. Griffa, M. Gough, and B. K. Haus (2014), Data assimilation considerations for improved ocean predictability during the Gulf of Mexico Grand Lagrangian Deployment (GLAD), *Ocean Model.*, *83*, 98–117.

Jones, C. E., B. B. Minchew, B. B. Holt, and S. S. Hensley (2011), Studies of the Deepwater Horizon oil spill with the UAVSAR radar, in *Monitoring and Modeling the Deepwater Horizon Oil Spill: A Record-Breaking Enterprise*, pp. 33–50, AGU, Washington, D. C.

Kalda, J., T. Soomere, and A. Giudici (2014), On the finite-time compressibility of the surface currents in the Gulf of Finland, the Baltic Sea, *J. Mar. Syst.*, *129*, 56–65.

Kurapov, A. L., J. S. Allen, G. D. Egbert, and R. N. Miller (2005), Modeling bottom mixed layer variability on the mid-Oregon shelf during summer upwelling, *J. Phys. Oceanogr.*, *35*(9), 1629–1649.

Maximenko, N., J. Hafner, and P. Niiler (2012), Pathways of marine debris derived from trajectories of Lagrangian drifters, *Mar. Pollut. Bull.*, *65*(1-3), 51–62, doi:10.1016/j.marpolbul.2011.04.016.

McGillicuddy, D. J., et al. (2007), Eddy/wind interactions stimulate extraordinary mid-ocean plankton blooms, *Science*, *316*(5827), 1021–1026.

McWilliams, J. C. (2008), The nature and consequences of oceanic eddies, in *Ocean Modeling in an Eddying Regime*, pp. 5–15, AGU, Washington, D. C.

Mensa, J. A., Z. Garraffo, A. Griffa, T. M. Özgökmen, A. Haza, and M. Veneziani (2013), Seasonality of the submesoscale dynamics in the Gulf Stream region, *Ocean Dyn.*, *63*(8), 923–941, doi:10.1007/s10236-013-0633-1.

Mied, R. P., R. A. Handler, and T. E. Evans (2000), Longitudinal convergence fronts in homogeneous rotating channels, *J. Geophys. Res.*, *105*(C4), 8647–8658.

Mied, R. P., R. A. Handler, and T. F. Donato (2002), Regions of estuarine convergence at high Rossby number: A solution in estuaries with elliptical cross sections, *J. Geophys. Res.*, *107*(C11), 3206, doi:10.1029/2001JC001050.

Munk, W., L. Armi, K. Fischer, and F. Zachariasen (2000), Spirals on the sea, *Proc. R. Soc. A*, *456*(1997), 1217–1280.

Niewiadomska, K., H. Claustre, L. Prieur, and F. d'Ortenzio (2008), Submesoscale physical-biogeochemical coupling across the Ligurian Current (northwestern Mediterranean) using a bio-optical glider, *Limnol. Oceanogr.*, *53*(5), 2210–2225.

Poje, A. C., T. M. Özgökmen, B. L. Lipphardt, B. K. Haus, E. H. Ryan, A. C. Haza, G. A. Jacobs, A. Reniers, M. J. Olascoaga, and G. Novelli (2014), Submesoscale dispersion in the vicinity of the Deepwater Horizon spill, *Proc. Natl. Acad. Sci. U. S. A.*, *111*(35), 12,693–12,698.

Pollard, R. T., and L. A. Regier (1992), Vorticity and vertical circulation at an ocean front, *J. Phys. Oceanogr.*, *22*(6), 609–625.
Schumacher, J., and B. Eckhardt (2002), Clustering dynamics of Lagrangian tracers in free-surface flows, *Phys. Rev. E*, *66*(1).
Shcherbina, A. Y., E. A. D'Asaro, C. M. Lee, J. M. Klymak, M. J. Molemaker, and J. C. McWilliams (2013), Statistics of vertical vorticity, divergence, and strain in a developed submesoscale turbulence field, *Geophys. Res. Lett.*, *40*, 4706–4711, doi:10.1002/grl.50919.
Thomas, L., and R. Ferrari (2008), Friction, frontogenesis, and the stratification of the surface mixed layer, *J. Phys. Oceanogr.*, *38*(11), 2501–2518.
van Sebille, E., M. H. England, and G. Froyland (2012), Origin, dynamics and evolution of ocean garbage patches from observed surface drifters, *Environ. Res. Lett.*, *7*(4), 044040, doi:10.1088/1748-9326/7/4/044040.
Yoder, J. A., S. G. Ackleson, R. T. Barber, P. Flament, and W. M. Balch (1994), A line in the sea, *Nature*, *371*(6499), 689–692.
Zhong, Y., and A. Bracco (2013), Submesoscale impacts on horizontal and vertical transport in the Gulf of Mexico, *J. Geophys. Res. Oceans*, *118*, 5651–5668, doi:10.1002/jgrc.20402.